

Constraining Merging Galaxy Clusters with X-ray and Lensing Simulations & Observations: The case of Abell 2146

Urmila Chadayammuri,^{1,2*} John ZuHone,¹ Paul Nulsen,¹ Daisuke Nagai,^{2,3}

Sharon Felix,⁴ Felipe Andrade-Santos,¹ Lindsay King,⁴ Helen Russell⁵

¹*Chandra X-ray centre, Smithsonian Astrophysical Observatory, 60 Garden Street, Cambridge, MA 02143, USA*

²*Department of Astronomy, Yale University, New Haven, CT 06511, USA*

³*Department of Physics, Yale University, New Haven, CT 06520, USA*

⁴*Department of Physics, University of Texas - Dallas, Richardson, TX 75080, USA*

⁵*School of Physics and Astronomy, University of Nottingham, Nottingham NG7 2RD, UK*

Accepted XXX. Received YYY; in original form ZZZ

ABSTRACT

Galaxy cluster mergers are a powerful laboratory for testing cosmological and astrophysical models. However, interpreting individual merging clusters depends crucially on their merger configuration, defined by the masses, velocities, impact parameters, and orientation of the merger axis with respect to the plane of the sky. In this work, we investigate the impact of merger parameters on the X-ray emitting intracluster medium and gravitational lensing maps using a suite of idealised simulations of binary cluster mergers performed using the GAMER-2 code. As a test case, we focus on modeling the Bullet Cluster-like merging system Abell 2146, in which deep *Chandra* X-ray and lensing observations revealed prominent merger shocks as well as the mass distribution and substructures associated with this merging cluster. We identify the most interesting parameter combinations, and evaluate the effects of various parameters on the properties of merger shocks observed by deep *Chandra* and lensing observations. We show that due to gravitational compression of the cluster halos during the merger, previous mass estimates from weak lensing are too high. The plane of the merger is tilted further from the plane of the sky than estimated previously, up to 30° from the plane of the sky. We discuss the applicability of our results to multi-wavelength observations of merging galaxy clusters and their use as probes of cosmology and plasma physics.

Key words: clusters: theory — clusters: simulation — cosmological simulations:general — cosmological simulations:sub-grid model — ICM — AGN

1 INTRODUCTION

Merging galaxy clusters are powerful astrophysical laboratories for studying cosmology and astrophysics. To date, merging galaxy clusters have provided unique constraints on the nature of dark matter (Markevitch et al. 2004; Clowe et al. 2006; Massey et al. 2015; Harvey et al. 2015; Massey et al. 2018) and on the plasma physics of the X-ray emitting intracluster medium (ICM; see Markevitch & Vikhlinin 2007; Zuhone & Roediger 2016, for reviews). Mergers are crucial to the hierarchical formation of galaxy clusters, and the frequency of mergers with different mass ratios depends on cosmology (Lacey & Cole 1993; Fakhouri et al. 2010). Spatial offsets between the collisionless stars, dissipative gas, and lensing mass in merging systems like the Bullet Cluster provide constraints on the cross-section of self-interaction of the dark matter (Randall et al. 2008; Kahlhoefer et al. 2014; Kim et al. 2017; Robertson et al. 2017; Tulin & Yu 2018, for a review). Shocks and cold fronts are also used to derive unique con-

straints on the microphysics of the ICM, such as the rate of electron-proton equilibration (Rudd & Nagai 2009; Avestruz et al. 2015; Wang et al. 2018), thermal conduction (Markevitch et al. 2003; ZuHone et al. 2013), and viscosity (Roediger et al. 2013; ZuHone et al. 2015; Schmidt et al. 2017); each of these in turn constrains the properties of cosmic magnetic fields (see e.g., Brunetti & Jones 2014, for a review).

Cosmological simulations yield distributions for the merger speed and dark matter concentrations of the halos (Neto et al. 2007; Duffy et al. 2008), which in turn provide priors for dynamical parameters for merging clusters. However, interpreting specific observed features associated with merging clusters is particularly challenging, because (a) the initial merger and structural parameters are unknown and (b) the systems are not in equilibrium (Golovich et al. 2016, 2017; Wittman et al. 2018). Understanding and controlling the effects of these parameters are crucial for using merging galaxy clusters as probes of cosmology and plasma physics.

Idealised simulations enable powerful, controlled experiments to explore the large space spanned by the cluster merger parameters as well as non-gravitational processes op-

* E-mail: urmila.chadayammuri@cfa.harvard.edu

erating during the cluster formation and evolution (Ricker & Sarazin 2001; Ritchie & Thomas 2002; Poole et al. 2006; ZuHone 2011). For example, the halo masses, infall velocity and impact parameter largely determine the curvatures and Mach numbers of the shocks. The observed features also depend critically on the direction from which the merging cluster is viewed. Pre-shock gas temperatures depend on the masses of the two substructures, as well as their initial gas profiles. The strength of a merger shock depends on the velocity of the perturbing subcluster core through the ICM of the primary cluster, and on the time, or merger phase, at which the system is observed (Zhang et al. 2019, 2020). Furthermore, the observed strength of a shock and the curvature of the shock front both decrease as our viewing direction deviates from the normal to the plane of the merger. Due to the large number of parameters and potential degeneracies between them, they cannot be determined analytically. It is necessary to explore the multi-dimensional parameter space with tailored simulations.

In this work, we use simulations to understand one of the best-observed merging galaxy clusters in the X-ray. The ICM of Abell 2146 was first observed with the *Chandra* X-ray Telescope in 2009 (Russell et al. 2010). This observation revealed some of the clearest merger shocks since the Bullet Cluster (Markevitch et al. 2002). Being less massive and thus cooler than the Bullet Cluster, the gas in Abell 2146 radiates in an energy range where the effective area of *Chandra* is higher, so that surface brightness and temperature can be mapped in unprecedented detail. Constraints on the mass ratio $R = M_2 : M_1$ of the system have been made in previous work using weak lensing and galaxy velocities (King et al. 2016; White et al. 2015), one projection angle was inferred from the line-of-sight velocity separation between galaxies in different subclusters, and infall velocities and time since pericentre passage have been estimated from the positions and Mach numbers of the two shocks in the X-ray (Russell et al. 2012).

In order to determine the parameters of the merger in Abell 2146, we perform a suite of idealised simulations of binary cluster mergers using the GPU-accelerated adaptive mesh refinement code GAMER-2 (Schive et al. 2018). We use the most quickly evolving observables to narrow down the times at which simulated mergers best match Abell 2146, and then assess the effects of the remaining parameters and viewing direction on the observable X-ray and lensing properties of the simulated clusters.

We describe the simulation setup and translation to observable quantities in §2. We present observational constraints from X-ray and lensing observations of A2146 in §3. We describe the parameter tests in §4, concluding with best fit parameters for Abell 2146 and summarize conclusions in §6. Throughout this paper we use the flat Planck Collaboration et al. (2016) cosmology with $H_0 = 67.7 \text{ km s}^{-1} \text{ Mpc}^{-1}$ and $\Omega_m = 0.307$. At the redshift of Abell 2146, $z = 0.2323$, this corresponds to an angular scale of 3.823 kpc/arcsec.

2 SIMULATIONS

The simulations were run with GAMER-2 (Schive et al. 2018), a GPU-accelerated Adaptive MESH Refinement code. The GPU acceleration allows us to simultaneously explore

the effect of an unprecedented number of distinct parameters. For this initial study, we use ~ 25 million dark matter particles, and use four levels of refinement to achieve a hydrodynamic resolution of 6.8 kpc. Each run takes 5 hours on the Nvidia Tesla K80 GPU nodes on the Grace cluster at the Yale High Performance Computing centre. The present suite of simulations models the dark matter and non-radiative gas. Here, we describe the initial conditions and set up of the merger simulations.

2.1 Dark matter and gas profiles

We model the initial dark matter distribution of a cluster with the “super-NFW” profile:

$$\rho(r) = \frac{3M}{16\pi a^3} \frac{1}{(r/a) \times (1+r/a)^{5/2}} \quad (1)$$

where the scale radius is related to the half-mass radius as $a = R_e/5.478$ (Lilley et al. 2018). This form has a finite total mass, which makes it preferable to the NFW profile for ensuring a smooth cutoff of the DM density at large radii. sNFW properties are related to those of the more widely used NFW profile as follows. The scale radius r_{sc} of a halo is defined as the radius where the logarithmic slope of the density profile is $d \log \rho / d \log r = -2$, and the concentration is defined as $c_{\text{NFW}} = r_v / r_{sc}$, where r_v the virial radius. For NFW halos, Duffy et al. (2008) measured the concentration-mass relation:

$$c_{\text{NFW}} = 5.74 \times \left(\frac{M}{2 \times 10^{12} h^{-1} M_\odot} \right)^{-0.097}, \quad (2)$$

where the distribution in c_{NFW} at fixed M is log-normal and the standard deviation of $\log_{10} c_{\text{NFW}}$ is 0.14. For the sNFW profile, $r_{sc} = 2a/3$ so that the concentration is $c_{s\text{NFW}} = r_v / r_s = 3r_v / 2a$. Fitting sNFW profiles with NFW formulae, Lilley et al. (2018) find that the concentrations in the two models are well-described by a linear fit, $c_{s\text{NFW}} = 1.36 + 0.76c_{\text{NFW}}$. Therefore, given an NFW concentration, we find the equivalent sNFW concentration, which then yields the scale radius a .

The gas is initially set up to be in hydrostatic equilibrium with the dark matter. This criterion alone, however, is insufficient to yield both temperature and density profiles. We therefore model the gas density with the modified beta profile of Vikhlinin et al. (2006), which, along with the condition of hydrostatic equilibrium, gives the temperature. These profiles have the form

$$n_p n_e = n_0^2 \frac{(r/r_c)^{-\alpha}}{(1+r^2/r_c^2)^{3\beta-\alpha/2}} \frac{1}{(1+r^\gamma/r_s^\gamma)^{\epsilon/\gamma}} \quad (3)$$

where n_e and n_p are the number densities of electrons and protons, respectively. The inner density slope α and the core radius r_c control the strength and extent of the cool core. The scale radius of the gas density, r_s , is independent from the sNFW scale radius a . At intermediate radii the slope of the density profile, in log-log space, is -3β , and outside r_s it transitions to $-(3\beta + \epsilon/2)$ over a length scale determined by γ . Once the total mass profile is set, the dark matter particles are given velocities that place them in virial equilibrium, using the procedure outlined in Kazantzidis et al. (2004), where the energy distribution function is calculated via the Edding-

ton formula (Eddington 1916):

$$\mathcal{F}(\mathcal{E}) = \frac{1}{\sqrt{8\pi^2}} \left[\int_0^{\mathcal{E}} \frac{d^2\rho}{d\Psi^2} \frac{d\Psi}{\sqrt{\mathcal{E}-\Psi}} + \frac{1}{\sqrt{\mathcal{E}}} \left(\frac{d\rho}{d\Psi} \right)_{\Psi=0} \right] \quad (4)$$

where $\Psi = -\Phi$ is the relative potential and $\mathcal{E} = \Psi - \frac{1}{2}v^2$ is the relative energy of the particle. We compute this distribution function and use it to determine DM particle speeds using the acceptance-rejection method. The direction of each particle's velocity is determined by choosing random unit vectors in \mathcal{R}^3 . The gas cell velocities are zero, i.e., the system is in hydrostatic equilibrium.

In §4.6, we explain how r_c was chosen to roughly match observations of relaxed cluster profiles. Since this study focuses on merger shocks, we do not vary the model parameters r_s/a , γ or ϵ , which affect the gas distribution on large scales. These would likely be relevant if the merger were more evolved and the shocks much further out, or in modeling a system with accretion shocks. Both these scenarios are outside the scope of the current work. We adopt $\beta = 2/3$, $\gamma = 3$ and $\epsilon = 3$, which were found to fit all the observed clusters in the Vikhlinin et al. (2006) sample, and set $r_s = a$.

2.2 Merger geometry

The merger evolution and observed properties depend on the impact parameter b and relative velocity v —their product L is the specific angular momentum of the subhalo. Initially, the primary halo sits on the x -axis and has a speed $v/2$ in the positive x direction. The centre of the subhalo is located in the x - y plane at $y = b$, with its x coordinate chosen to make the distance between the two centres 3 Mpc, comparable to the sum of the virial radii. The subhalo is set in motion at speed $v/2$ in the negative x direction. This is shown schematically in Fig. 1.

For two halo masses M_1 and M_2 , the approximate infall velocity can be analytically estimated by considering the turnaround radius d_0 where the relative radial velocity is 0, as shown in (Sarazin 2002):

$$d_0 \simeq 4.5 \text{ Mpc} \times \left(\frac{M_1 + M_2}{10^{15} M_\odot} \right)^{1/3} \times \left(\frac{t_{\text{merge}}}{10^{10} \text{ yr}} \right)^{2/3} \quad (5)$$

$$v \simeq 2930 \text{ km/s} \left(\frac{M_1 + M_2}{10^{15} M_\odot} \right)^{1/2} \left(\frac{d}{1 \text{ Mpc}} \right)^{-1/2} \left[\frac{1 - \frac{d}{d_0}}{1 - \left(\frac{b}{d_0} \right)^2} \right]^{1/2} \quad (6)$$

where d is the separation between the halo centres at the beginning of the simulation, b is the impact parameter, and t_{merge} is the age of the Universe at the time of the merger. Since Abell 2146 is observed at $z = 0.2323$ and is close to pericentre passage, we use $t_{\text{merge}} = 10.8$ Gyr. The infall velocity, on average, then ranges from 720 - 1220 km/s for the range of halo masses explored.

Neither the infall velocity nor the impact parameter is directly observable post-merger, and the separations and velocities they do produce are observed in projection. Assuming that the two BCGs in the field trace the potential minima of the two clusters, White et al. (2015) constrained the merger plane to be tilted 13-19° from the plane of the sky. The observed shock velocity, 2200 km/s for the bow shock, is higher than the initial velocities, since the halos and the

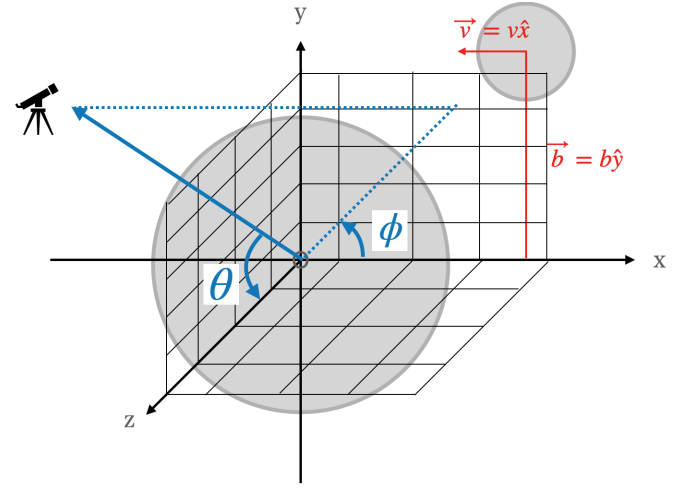


Figure 1. Schematic of initial configuration. The relative velocity between the subclusters is in the x direction, with an initial impact parameter b along the y direction; the merger thus occurs in the x - y plane. The observer is in the direction of the telescope, so that the viewing direction is determined by the polar angle θ and the azimuthal angle ϕ .

gas in them accelerate under gravity; this point was crucial in the interpretation of the Bullet Cluster, which was otherwise considered an anomaly within Λ CDM (Springel & Farrar 2007; Lage & Farrar 2015). The X-ray observations suggest a small, non-zero impact parameter (Russell et al. 2010), but cannot constrain it directly. We test a range of values from 50-700 kpc and assess how it affects the X-ray features.

To summarise, the initial cluster velocities are along the x -axis, the impact parameter along the y -axis, and the default line-of-sight is the z -axis, $(0, 0, 1)$. If the viewing direction is defined by the polar and azimuthal angles (θ, ϕ) , images we see will be projections of the simulation box along the normal

$$\mathbf{n} = [\sin \theta \cdot \cos \phi, \sin \theta \cdot \sin \phi, \cos \theta]. \quad (7)$$

Thus, if the 3D separation between the halo centres is \mathbf{d} and their 3D relative velocity is \mathbf{v} , the observed separation and relative line-of-sight velocity are given by $d_{\text{proj}} = \sqrt{\mathbf{d}^2 - (\mathbf{d} \cdot \mathbf{n})^2}$ and $v_{\text{los}} = -\mathbf{v} \cdot \mathbf{n}$.

3 CONSTRAINING CLUSTER MERGER MODELS USING X-RAY AND LENSING OBSERVATIONS

In this work, we focus on modeling multi-wavelength observations of Abell 2146, consisting of X-ray observations (Russell et al. 2010; Russell et al. 2012), spectroscopic data on the bright galaxies (White et al. 2015), and strong+weak lensing measurements (King et al. 2016; Coleman et al. 2017). The details of each observation can be found in the corresponding papers. Below, we highlight the salient features of these observations that are relevant to the merger and structural parameters of A2146. The quantitative constraints are summarised in Table 1.

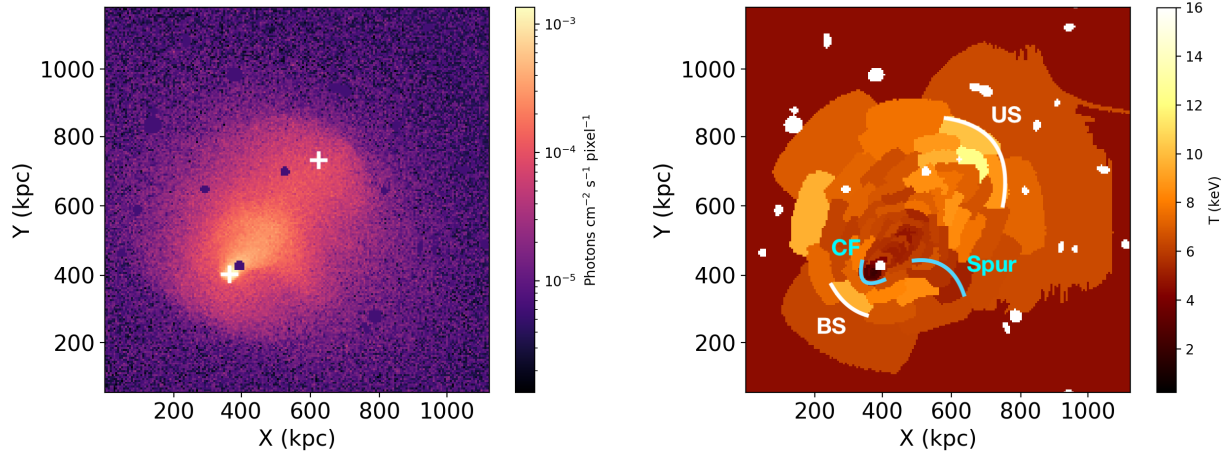


Figure 2. X-ray surface brightness (left) and temperature (right) maps of Abell 2146, reproduced from the *Chandra* archive. The BCGs A2146-A and A2146-B identified and used in optical and lensing studies are marked as white crosses on the surface brightness map. The bow shock and upstream shock are highlighted in white, and the cold front and plume in blue, on the temperature map. The black areas in the surface brightness and corresponding white areas in the temperature map are where bright point sources were masked.

3.1 The *Chandra* data

We use the 419.5 ks of ACIS observations of A2146 from the *Chandra* archive. The data were reduced using the `chav` software package¹ with CIAO v4.6 (Fruscione et al. 2006), following the processing described in Vikhlinin et al. (2005) and applying the CALDB v4.7.6 calibration files. The X-ray surface brightness map has a resolution of 1", corresponding to 3.7 kpc at the cluster redshift $z_c = 0.2323$. The temperature maps are coarser, since it is necessary to bin several pixels together to get enough photons to fit a spectrum. Therefore, we use the surface brightness maps to identify sharp features in the ICM, and then infer from the temperature maps whether they are shock or cold fronts.

3.1.1 Shock fronts

A shock is an abrupt increase in both temperature and density occurring when a perturber - in this case, the infalling subcluster - moves through an ambient medium, creating and propagating a compressive disturbance. Unlike in an adiabatically compressed region, the entropy in a shock is increased. Abell 2146 features two of these - a bow shock with a Mach number $\mathcal{M} = 2.3 \pm 0.2$, and an upstream shock of $\mathcal{M} = 2.1 \pm 0.1$ (Russell et al. 2012, Russell et al. in prep.). The two have slightly different formation channels, and reproducing both simultaneously is a strong constraint on our simulations. As elaborated in §3.2, the merger produces other shocks too, although these are too weak to be detected by current X-ray telescopes.

Bow shocks form in front of the perturber, with the leading edge perpendicular to its direction of motion. The upstream shock is a reverse shock that forms ahead of the centre of the primary cluster. As the subcluster falls in, its halo gas is impeded by the ICM of the primary cluster and slows down. Gas stripped from around the leading edge of the merging subcluster forms an obstacle to the gas falling in its wake. The

resulting pressure disturbance travelling into the wake then develops into a shock propagating upstream into the wake. We note that this shock is distinct from the leading shock that propagates away from the initial contact discontinuity through the subcluster.

The bow shock forms first, followed shortly by the upstream shock. For each shock, the Rankine-Hugoniot jump conditions yield the Mach number, which along with the distance travelled provides an estimate of the age of the shock. Russell et al. (2012) used this method to place the system at 0.1-0.3 Gyr post pericentre passage. The relation between the shock strength and age, however, is non-trivial for realistic cases where the perturber is not a rigid object, but rather a diffuse cluster that gets stripped and deformed over time (Zhang et al. 2019). The distance between the two shocks evolves rapidly following pericentre passage. This is therefore our preferred indicator of dynamical stage.

In the optically thin ICM, a shock front only appears as a sharp feature where it is nearly tangent to our lines-of-sight. What we observe is the projection of the emission per unit volume along the line-of-sight. A shock front generally curves away from the direction of propagation. Sight lines outside the shock intersect only unshocked gas. Sight lines inside the shock intersect some shocked gas, and the depth of the shocked gas increases as the line moves further inside the front. The abrupt edge is due to the depth of the sight line within the shocked gas varying with distance, x , behind the front as \sqrt{x} , for small x . Only the component of the gas velocity perpendicular to the shock front is affected by the shock, so that the shock is generally strongest at its leading edge and weakens towards the periphery of the curved shock front, where the front is inclined to its direction of motion. As a result, the standoff distance between the shock and the cold front marking the boundary of the remnant gas core is smallest at the leading edge of the shock and increases towards the periphery. This causes the observed standoff distance to depend on viewing direction, increasing as our lines-of-sight tilt away from the normal to the plane of the merger (see

¹ <http://hea-www.harvard.edu/~alexey/CHAV/>

Markevitch & Vikhlinin 2007, for a more detailed review of these effects).

The preshock temperature for the bow shock is close to the initial temperature of the gas at the appropriate radius in the primary cluster. The potential minimum of the primary cluster, like its observed BCG, lie within the upstream shock. The pre-shock temperature of the upstream shock, on the other hand, is that of high entropy gas from the outskirts of the subcluster, which has been subject to substantial adiabatic compression as it flowed into the central region of the primary cluster.

The strength of the bow shock depends on the movement of the perturber (i.e., the substructure core) through the ICM. This depends on the initial velocity, as well as on its gravitational acceleration due to the masses of the two halos, which in turn is larger if the impact parameter is lower. For the upstream shock, the velocity difference is between the gas stripped from the leading edge of the substructure, and the rapidly infalling gas from its outskirts.

Given the above considerations, constraints on initial velocity, masses, impact parameter and projection angles can only be inferred once the correct snapshot, i.e., dynamical phase, has been identified. Since the shock separation is the most rapidly evolving observable, we use that to select suitable snapshots.

3.1.2 Cold fronts

Unlike shock fronts, cold fronts are discontinuities where the temperature decreases as the density increases; in merging clusters, these are usually the remnants of cool cores (Markevitch & Vikhlinin 2007). If the merger were perfectly head on, the two cores would strongly disrupt, so that any cool core remnants feature would be very spread out. Furthermore, the two disrupting cores would be elongated along the same axis, that of the merger. Abell 2146 has an obvious cold front associated with BCG-A, a bullet-like subcluster punching through the ICM of the larger primary cluster, and a second, less striking discontinuity perpendicular to the axis between the shocks. These two are highlighted with blue curves in the temperature map of Fig. 2. The second feature has been called the "plume" in the X-ray observations, which also suggested that this is most likely the disrupted gas core of the primary halo (Russell et al. 2012). Such a configuration of cold features requires a non-zero impact parameter. If the impact parameter is too large, the substructure remnant will curve significantly towards the merger axis and towards the primary core, but never pass through any part of it directly. The two cool cores would thus be left relatively intact. Thus we can constrain the impact parameter using the brightness, width, and relative orientation of the two cold features.

3.2 The origin of observable merger features

Fig. 3 shows snapshots illustrating the development of the observed features. These have been described in detail in Roettiger et al. (1996, 1997); Takizawa (2005); Poole et al. (2006). Here, we present a brief summary to develop physical intuitions into the effects of the explored parameters. Illustrative snapshots are shown in Fig. 3. In the first panel, we see that as the subcluster falls in from the right, high entropy-gas from

Table 1. Summary of observed constraints for Abell 2146.

$M_{\text{tot,lens}}^{\dagger}$	$1.01 - 1.36 \times 10^{15} M_{\odot}$
$d_{\text{BS-US}}^{*,1}$	700 kpc
$d_{\text{BS-CF}}^{*,2}$	140 kpc
$(T_f, T_i)_{\text{BS}}^{*,3}$	(10, 5) kpc
$(T_f, T_i)_{\text{US}}^{\ddagger}$	(12, 6) kpc
$\Delta v_{\text{rel}}^{\ddagger}$	763 km s ⁻¹

[†] King et al. (2016)

^{*} Russell et al. (2012)

[‡] White et al. (2015)

¹ Shock separation, i.e., distance between the points of maximum curvature of the bow and upstream shocks.

² Standoff distance, i.e., distance between points of maximum curvature of the bow shock and cold front.

³ Pre- and post-shock temperature for the bow shock.

⁴ Pre- and post-shock temperature for the upstream shock, from Russell et al. in prep.

the outskirts of the two clusters is compressed into a high-temperature region around the contact discontinuity. This is enveloped by an extended, weakly shocked region. The centre of the subcluster, and therefore its BCG, originally lies outside this shocked region, but accelerates toward the shocked region as the rightward shock moves towards it, so that it eventually enters the shocked region. The subhalo core overtakes and passes through the initial contact discontinuity, and drives a shock behind the leftward moving shock. This is seen as the yellow-white, hottest region in the middle temperature panel. As the subcluster core undergoes pericentre passage, these two shocks connect, creating the appearance of prominent bulge near the centre of the large-scale front. This bulge is the feature identified as the bow shock in the observations. The pre-shock temperature ahead of this bow shock is that of the ICM of the primary halo. There is a second contact discontinuity between the cool core of the subcluster and the shocked ICM of the primary cluster, which is the cool core of the subcluster being elongated by ram pressure; this is what Poole et al. (2006) call a 'comet-like tail', and is seen in both the Bullet Cluster (Markevitch et al. 2002) and Abell 2146. Some gas stripped from the remnant subcluster core obstructs higher velocity gas falling to the left, in the wake of the subhalo, leading to the formation of the upstream shock, seen clearly in the third panel. The pre-shock gas here is from the outskirts of the subcluster, so that it has a relatively high entropy and adiabatic compression heats it well above its initial temperature. The core of the primary cluster is disrupted; this low entropy gas gets ejected perpendicular to the cold front from the subcluster core, forming the feature called a plume by Poole et al. (2006).

Eventually, the subcluster core turns around, whereas the shocks continue to move outwards. In our simulations, as in Poole et al. (2006), this happens ~ 1 Gyr after the first pericentre passage. However, the shocks at this point are too weak and extended to be comparable to systems like Abell 2146. Therefore, we focus on what can be learned from mergers in the first 0.5 Gyr after pericentre passage, while their morphology resembles that of Abell 2146 and the Bullet Cluster.

We treat the brightest cluster galaxies (BCGs) as tracers of the gravitational potential minima of the two merging clusters. The optical observations, used to determine positions and velocities of the BCGs, have *Hubble's* diffraction-limited

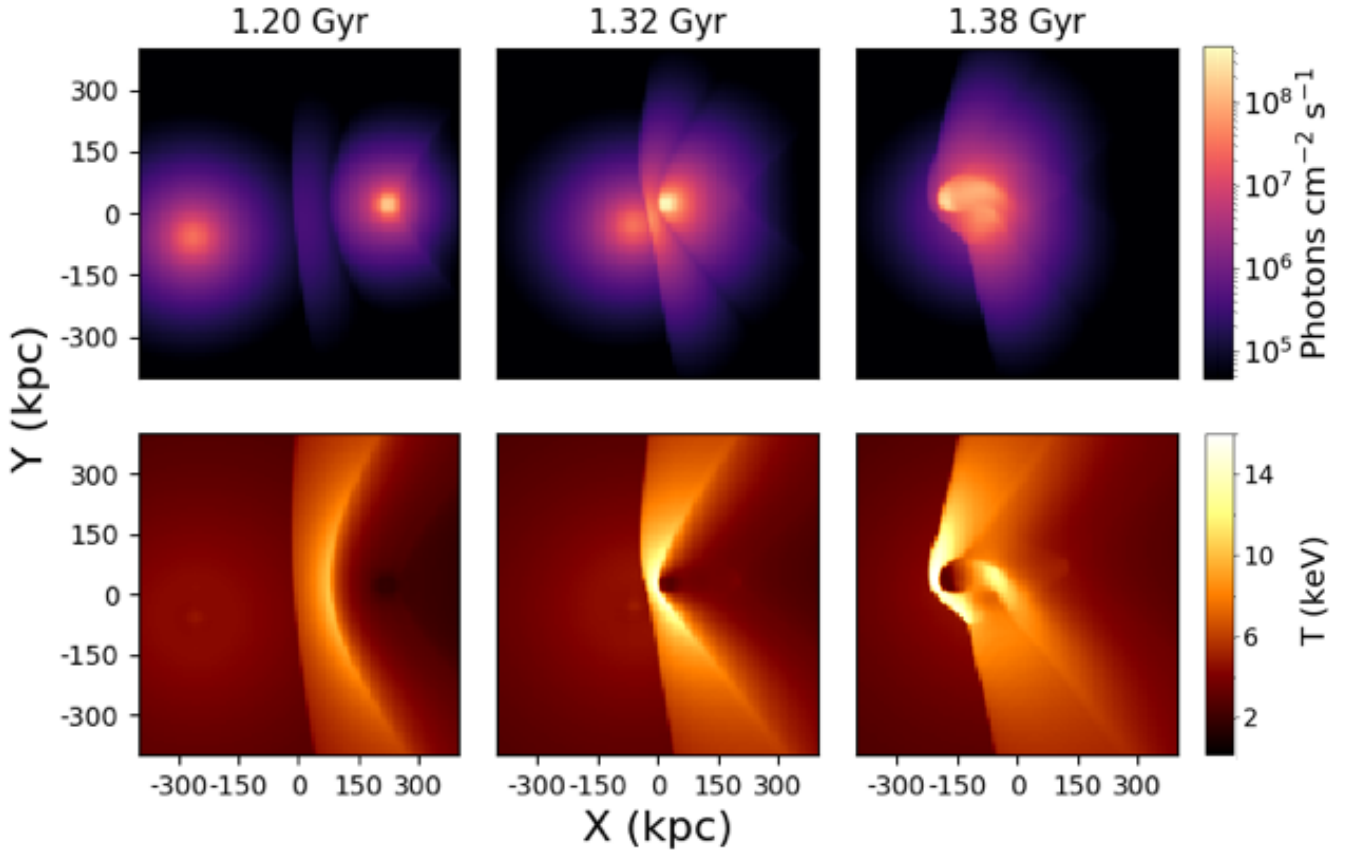


Figure 3. Snapshots of the surface brightness (top) and Mazzotta-weighted projected temperature (bottom) maps around the pericentre passage of the subcluster through the primary cluster, illustrating the development of the observed X-ray features. The first panel shows the initial contact discontinuity (i.e., a cold front), surrounded by one weak shock traveling towards the left and another towards the right. Pericentre passage occurs just before the middle panel, and the substructure core here creates an additional bow shock and contact discontinuity. By the final panel, subcluster gas that had been swept upstream by ram pressure meets gas that is still infalling, creating the upstream shock. The remnant of the primary cluster core is ejected almost perpendicular to the axis between the bow and upstream shocks, and is called the "plume" in observations.

resolution of $0.05''$ or ~ 0.18 kpc. Spectroscopic data is available for 63 of the brightest galaxies in the clusters (White et al. 2015), which yields line of sight velocities with uncertainties of less than 1%. We note that BCGs do not generally lie exactly at the potential minima of their host clusters, especially not in the midst of a merger. The relation between the BCG and cluster core velocities, therefore, is significantly less precise.

There is a clear BCG in the bullet-like cold front, referred to in the literature as BCG-A and treated as the BCG of the primary cluster referred to as Abell 2146-A (e.g., Canning et al. 2012; White et al. 2015; King et al. 2016; Coleman et al. 2017). These studies have assumed that the second brightest galaxy in the field, shown in the left panel of Fig. 2 near the upstream shock, is the BCG of the secondary cluster; this has been called BCG-B. Instead, our simulations consistently show that BCG-A must be associated with the secondary cluster, and BCG-B with the primary cluster, in order to reproduce the X-ray features.

3.3 Mass Profiles from Lensing Data

Weak lensing maps offer complementary constraints on the total mass and mass profiles of Abell 2146. These rely on measurements of the distortion of shapes of background galaxies in deep imaging with the *Hubble Space Telescope* (*HST*) (King et al. 2016). The observed ellipticity of a background galaxy (ϵ) depends on the intrinsic ellipticity (ϵ_i), as well as the (complex) reduced shear from the the cluster lens (g):

$$\epsilon = \epsilon_i + g = \epsilon_i + \frac{\gamma}{1 - \kappa}, \quad (8)$$

where γ and κ are the (complex) cluster shear ($\gamma \equiv \gamma_1 + i\gamma_2$) and convergence, respectively. The convergence is given by $\kappa = \Sigma/\Sigma_{cr}$, where Σ is the surface mass density of the lens, and Σ_{cr} is the critical surface mass density

$$\Sigma_{cr} = \frac{c_v^2 D_s}{4\pi G D_{ds} D_d}, \quad (9)$$

which depends on the angular diameter distances to the source D_s , to the lens D_d , and between the two, D_{ds} . The speed of light is denoted by c_v . κ and γ depend on the second

derivatives of the lensing potential ψ :

$$\kappa = \frac{1}{2}(\psi_{,11} + \psi_{,22}) \quad (10)$$

and

$$\gamma_1 = \frac{1}{2}(\psi_{,11} - \psi_{,22}) \quad (11)$$

$$\gamma_2 = \psi_{,12}. \quad (12)$$

In the weak lensing regime, $\kappa \ll 1$ and $|\gamma| \ll 1$.

A strong lensing analysis of the multiple images shows that the mass peaks at the brightest galaxy in the bullet-like cold front, BCG-A (Coleman et al. 2017). The parametric models considered in the weak lensing analysis had NFW components centred on the BCGs A and B, simultaneously fit to the lensing reduced shear data (ellipticities of the distant galaxies) (King et al. 2016). The free parameters were the two cluster radii r_{200} or, equivalently, masses enclosed inside r_{200} , M_{200} . The field-of-view of the data (~ 750 kpc at the system redshift) is not sufficient to simultaneously fit the cluster concentrations and masses. Therefore, the concentrations of the two clusters were fixed for each parametric fit, and were set to be equal to one another and in the range expected from the cluster mass-concentration relationship (Duffy et al. 2008). For $c = 4$, the total virial mass of the clusters is $M_{200} = 1.2 \times 10^{15} M_\odot$, and their mass ratio is ≈ 4 . The total mass is about 10% bigger for $c = 3.5$ and 10% smaller for $c = 4.5$. In the weak lensing analysis, Abell 2146-A, centred on BCG-A, is the more massive cluster. Instead, our simulations suggest the opposite to be the case - the deeper potential minimum, associated with the primary cluster, resides in the upstream shock, like the observed BCG-B.

In order to fit projected mass density profiles to the simulation data, or obtain synthetic shear maps, we must project the total 3D mass in the simulation boxes along the line of sight to obtain Σ or κ . Assuming that the gravitating mass profile of each cluster is well described by the NFW model (Navarro et al. 1996), we can then simultaneously fit projected NFW profiles (Lokas & Mamon 2001) centred on the two potential minima to the projected mass using

$$\Sigma(R) = \frac{c^2}{2\pi} g(c) \frac{M_v}{r_v^2} \cdot \frac{1 - |c^2 \tilde{R}^2 - 1|^{-1/2} C^{-1} \left[\frac{1}{c\tilde{R}} \right]}{c^2 \tilde{R}^2 - 1}, \quad (13)$$

where $c = c_{\text{NFW}}$, $\tilde{R} = R/r_v$, R is the projected distance from the centre and

$$g(c) = \frac{1}{\ln(1+c) - \frac{c}{1+c}},$$

$$C^{-1}(x) = \begin{cases} \cos^{-1}(x), & \text{if } R > r_s \\ \cosh^{-1}(x), & \text{if } R < r_s. \end{cases}$$

Roediger & Zuhone (2012) have shown that the observed mass of a subcluster within a given radius can vary dramatically over the course of a merger (though they only examined a single simulation with a large impact parameter). The gravitational potential deepens, and includes the mass of both systems near pericentre, so that during pericentre passage the measured concentration would be substantially larger than pre-merger. When the system eventually virialises again with the combined mass of the two halos, the total concentration is lower than pre-merger, consistent with the concentration-mass relation.

There is a degeneracy between mass and concentration in weak lensing observations, such that assuming a lower concentration requires a higher mass to produce the same convergence κ . Furthermore, lensing observations do not sample the full density field - rather, they provide local measurements of the reduced shear $\gamma/(1-\kappa)$ at the positions of background galaxies. For Abell 2146, King et al. (2016) had ~ 1500 such shape measurements. The limited number of galaxies per radial bin combines with the shape noise, i.e. inherent dispersion in the unlensed distribution of shapes for the background galaxies, to restrict the signal-to-noise ratio. Lastly, as noted above, the field of view of the HST observations did not extend to the outskirts of the cluster system. As a result, it was unfeasible to simultaneously fit the dark matter concentration and total mass/virial radius of each cluster. Therefore, the lensing analysis focused on a range of concentrations $3.5 \leq c_{\text{NFW}} \leq 4.5$, motivated by the concentration-mass relation (e.g., Duffy et al. 2008), and then fit the virial radius for each c_{NFW} . These masses are 50-100% higher than those from X-ray and SZ observations.

The concentrations of merging halos, however, are systematically different from those of their relaxed counterparts. We found that initial concentrations of $3 < c_{\text{NFW}} < 6$ for either halo, a range broader than the $1-\sigma$ scatter in the $c-M$ relationships at cluster masses, was consistent with the X-ray observations. We then created maps of the projected density at 8 snapshots around the one that best fit the X-ray observations, capturing the 0.2 Gyr centred on core passage. At each snapshot, the projected density was sampled at $\approx 60,000$ points and projected NFW density profiles were simultaneously fit to this sampling. The results of these fits are shown in the top panel of Fig. 4, where the initial values were $c_1 = c_2 = 5$ (corresponding to clusters referred to as Abell 2146-B and Abell 2146-A respectively in the lensing papers). Assuming that a spherically symmetric NFW profile is a good description for the haloes even this close to core passage, the best-fit c_{NFW} is biased high, particularly for the less massive subcluster. Consistent with the results of Roediger & Zuhone (2012), c_{NFW} peaks at pericentre passage and then decreases over time. Even 0.1 Gyr after pericentre passage, the fit concentrations are 20% higher than the initial values.

To illustrate and quantify the mass error due to the assumption of particular concentration values when fitting parameterised lens models, we created shear maps using a Fast Fourier Transform (FFT), and lensed synthetic background galaxy populations with galaxy number density set to match the observed *HST* field. As was done in the lensing papers, we assume different values for c_{NFW} and fit only for the virial mass M_{200} . The upper panel of Fig. 5 shows the results for haloes of mass $M_1 = 5.0 \times 10^{14} M_\odot$ and $M_2 = 1.6 \times 10^{14} M_\odot$ and concentrations $c_1 = c_2 = 5$. Fit distributions are shown when $c = 3$ is assumed for each halo. Results for the lower (higher) mass halo are shown in orange (blue), with a vertical line indicating the true mass. To demonstrate the impact of adopting a particular concentration, the bottom panel shows the results of such a lensing forward model for a halo mass $M = 1.6 \times 10^{14} M_\odot$ and $c = 5.0$, i.e., the best fit initial NFW parameters for the less massive subcluster. For 100 different realizations of background galaxy positions and ellipticities, the orange, green and red curves show the distributions of

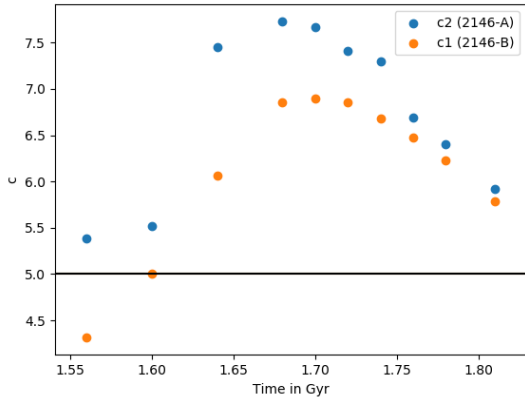


Figure 4. The evolution with time of the dark matter concentration parameter for NFW haloes fit to the simulated projected (dark matter) density. In this case, the clusters have initial true total masses $M_1 = 5 \times 10^{14} M_\odot$ and $M_2 = 1.6 \times 10^{14} M_\odot$ and concentrations $c_1 = c_2 = 5$ respectively as indicated by the horizontal line.

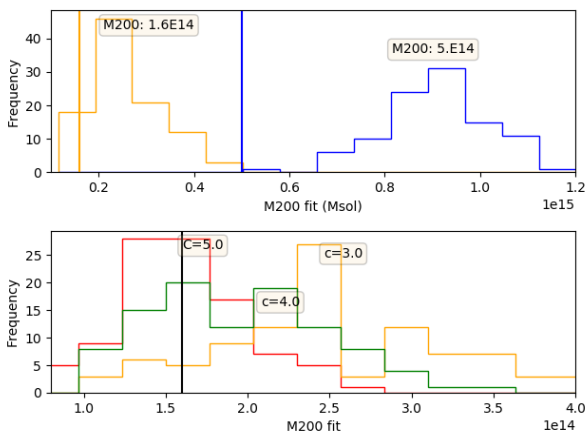


Figure 5. Upper panel: The distribution of masses for NFW haloes fit to synthetic lensing catalogues, generated using haloes with true masses $M_1 = 5.0 \times 10^{14} M_\odot$ and $M_2 = 1.6 \times 10^{14} M_\odot$ and concentrations $c_1 = c_2 = 5$. Fit distributions are shown when $c = 3$ is assumed for each halo. Results for the lower (higher) mass halo are shown in orange (blue), with a vertical line indicating the true mass. The masses are overestimated by $\sim 50\%$ for the less massive halo, and $\sim 85\%$ for the more massive halo. Lower panel: The distribution of masses for NFW haloes fit to synthetic lensing catalogues, generated using a halo with $M_2 = 1.6 \times 10^{14} M_\odot$, $c_2 = 5$. Fit distributions are shown when $c = 3$ (orange), $c = 4$ (green) and $c_2 = 5$ (red) are assumed. The true halo mass is indicated with a black vertical line.

the fit mass M_{200} assuming $c = 3$, $c = 4$ and $c = 5$ while fitting respectively.

Note that assuming concentrations lower than the true value biases mass high. During model fitting, as noted above, King et al. (2016) focused on concentrations in the range (3.5–4.5) for the clusters in the system, and correspondingly obtained a higher mass, $(1.0–1.3) \times 10^{15} M_\odot$ than would have been obtained when adopting higher concentrations, which is consistent with our analysis. However, as noted in King et al.

Observable	Simulated Analogue
Surface brightness	Emission-weighted projected photon emissivity in 0.3-7 keV
Temperature	Mazzotta-weighted projected temperature
Lensing	Projected density map
Galaxy spectra	Average velocity of dark matter particles in 50 kpc radius (BCG) or 1 Mpc (cluster average)

Table 2. Summary of the simulated analogues to observed quantities

(2016), in order for the lensing data to yield a mass for Abell 2146-A similar to that of Abell 2146-B, Abell 2146-A would have to have $c_1 \sim 9$ when $c_2 \sim 3.5$ for Abell 2146-B.

A key lesson from this exercise is that lensing masses, especially from parametric reconstruction, are degenerate with the assumed concentrations. Ideally, there would be sufficient signal-to-noise and field-of-view in the lensing data to constrain both simultaneously. But this is very rare in space-based lensing observations. Instead, the robust, model-independent quantity from lensing surveys is the reduced shear measured from the distant galaxy ellipticities. Comparisons between cluster mass model parameters from simulations and from observations must therefore be made by forward modeling the simulations and fitting their shear maps to the same parametric mass models, under the same observational conditions, such as field-of-view, galaxy number density available for shear measurements etc.

The simulated analogs to observable quantities are summarised in Table 2.

4 RESULTS

The primary goal of this work is to investigate how the observed properties of A2146 depend on the parameters of the simulation. To this end, we compare simulations where all parameters are held constant except the one in consideration, and choose snapshots where the shock separation meets this observed constraint. For all sections but that on the viewing direction in §4.2, the system is viewed along the z axis, perpendicular to the plane of the orbit.

4.1 Initial Cluster Merger Setup

Since the mass ratio of this merger derived from weak lensing has a large uncertainty due to the restricted field-of-view and the necessity to assume concentration parameters, we constrained this parameter by examining simulations from the Galaxy Cluster Merger Catalog (Zuhone et al. 2018).² This allows us to inspect mock observations of quantities such as projected X-ray surface brightness, spectral-like weighted temperature following Mazzotta et al. (2004) (henceforth Mazzotta-weighted), and total mass density for a range of mass ratios and impact parameters in binary merger simulations. Using the simulation set ‘‘A Parameter Space Exploration of Galaxy Cluster Mergers’’ in the Galaxy Cluster Merger Catalog³ (Zuhone et al. 2011), we identified a region

² <http://gcmc.hub.yt>

³ <http://gcmc.hub.yt/fiducial/index.html>

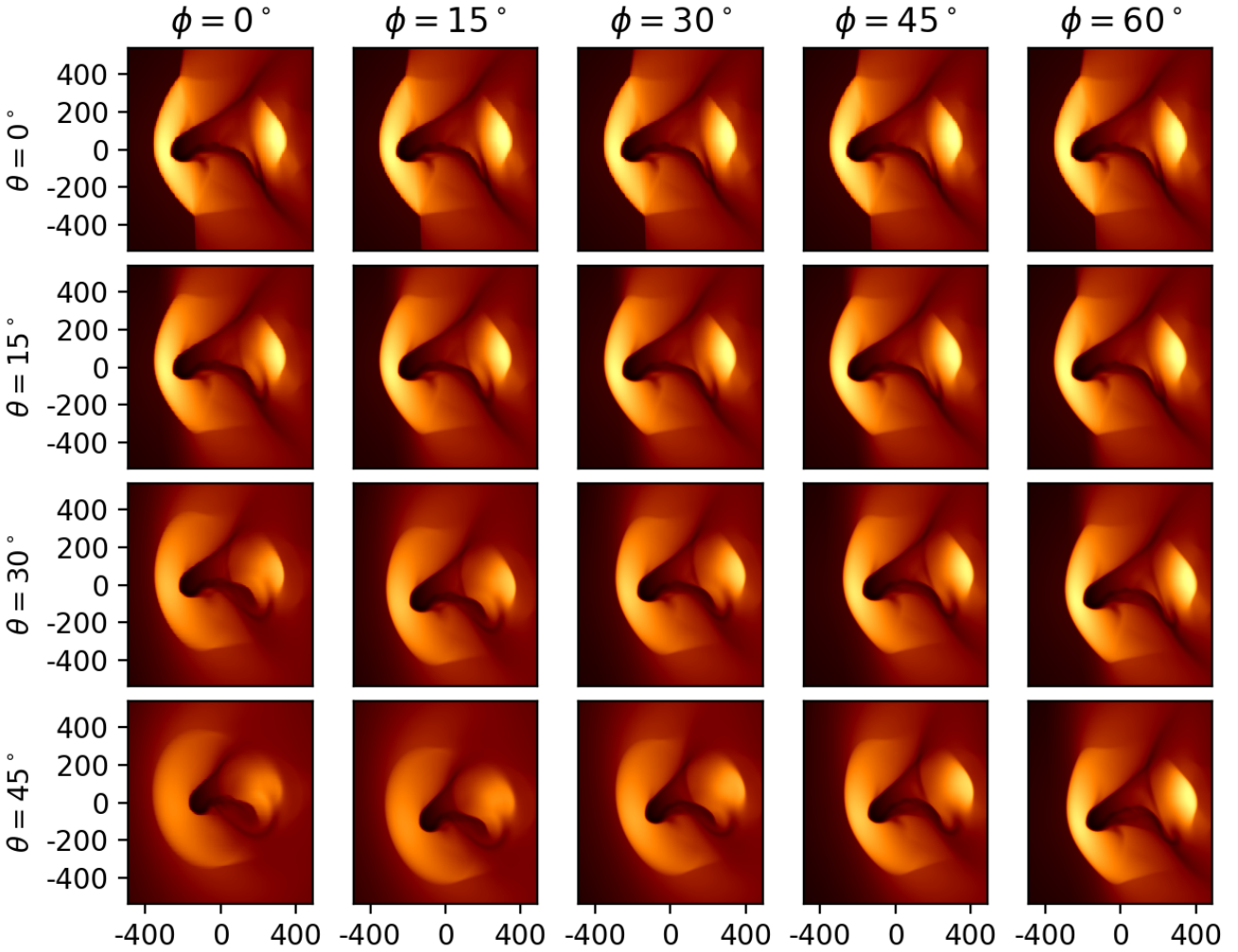


Figure 6. The effect of changing the viewing angles (θ , ϕ). Mazzotta-weighted projected temperature maps for the simulation with $M_1 = 5 \times 10^{14} M_\odot$, $R = 1 : 3$, $b = 100$ kpc, $v_{\text{rel}} = 1452$ km/s. Any viewing angle that is not perpendicular to the plane of the merger will cause weaker apparent shocks. Each panel is 800 kpc a side, and the colormap is the same as for all simulated temperature maps. We find that shocks are visible from every viewing direction shown here, i.e., visibility of shocks is not a guarantee of a nearly plane-of-sky merger.

of parameter space to explore further to find an analog for Abell 2146. If the subhalo is very close in mass to the primary halo, the system would look more symmetric; if the mass of the subhalo is too small, the cold front would be much weaker and the core of the primary halo is barely disrupted. If the impact parameter is close to zero, both cores are extremely disrupted and the standoff distance between the bow shock and cold front is too big; if it is too large, the cold remnant core of the subhalo appears extremely curved as the cores accelerate towards each other. Lastly, for the cold front and both shocks to be prominent, the observation must have occurred shortly after first pericentre passage. The X-ray features of Abell 2146 were qualitatively similar to the mergers with a mass ratio of 1:3 and a small, non-zero impact parameter, seen (0.3-0.5) Gyr post pericentre passage. In this work, we will explore more finely around this position in parameter space, and additionally study the effects of varying dark matter and gas profiles of the halos, relative velocity, and viewing direction.

If the BCGs are relatively good tracers of the potential minima, the orientation of the merger is well-constrained by the angles (θ , ϕ) for which the 3D separation and relative velocities of the potential minima in the simulation match observations after projection. The projected maps of surface brightness, temperature and mass should be made for the appropriate viewing direction to compare with observations.

In addition to the BCGs, we can also use the separation between the bow and upstream shocks, which evolves rapidly, to identify a small number of snapshots for further inspection. As shown in Fig. 6, we find that the shocks appear too weak if $\theta \gtrsim 30^\circ$ and $\phi \gtrsim 30^\circ$. The observed separation between the leading edges of the two shocks is 440 kpc (Russell et al. 2010). Therefore, we only keep snapshots where $440 < d < 508$ kpc, where the upper bound ensures that $d \cos 30^\circ \leq 440$ kpc.

The purpose of this study is to investigate how observed properties of the system depend on each of the input parameter of the simulation. Through a preliminary round of param-

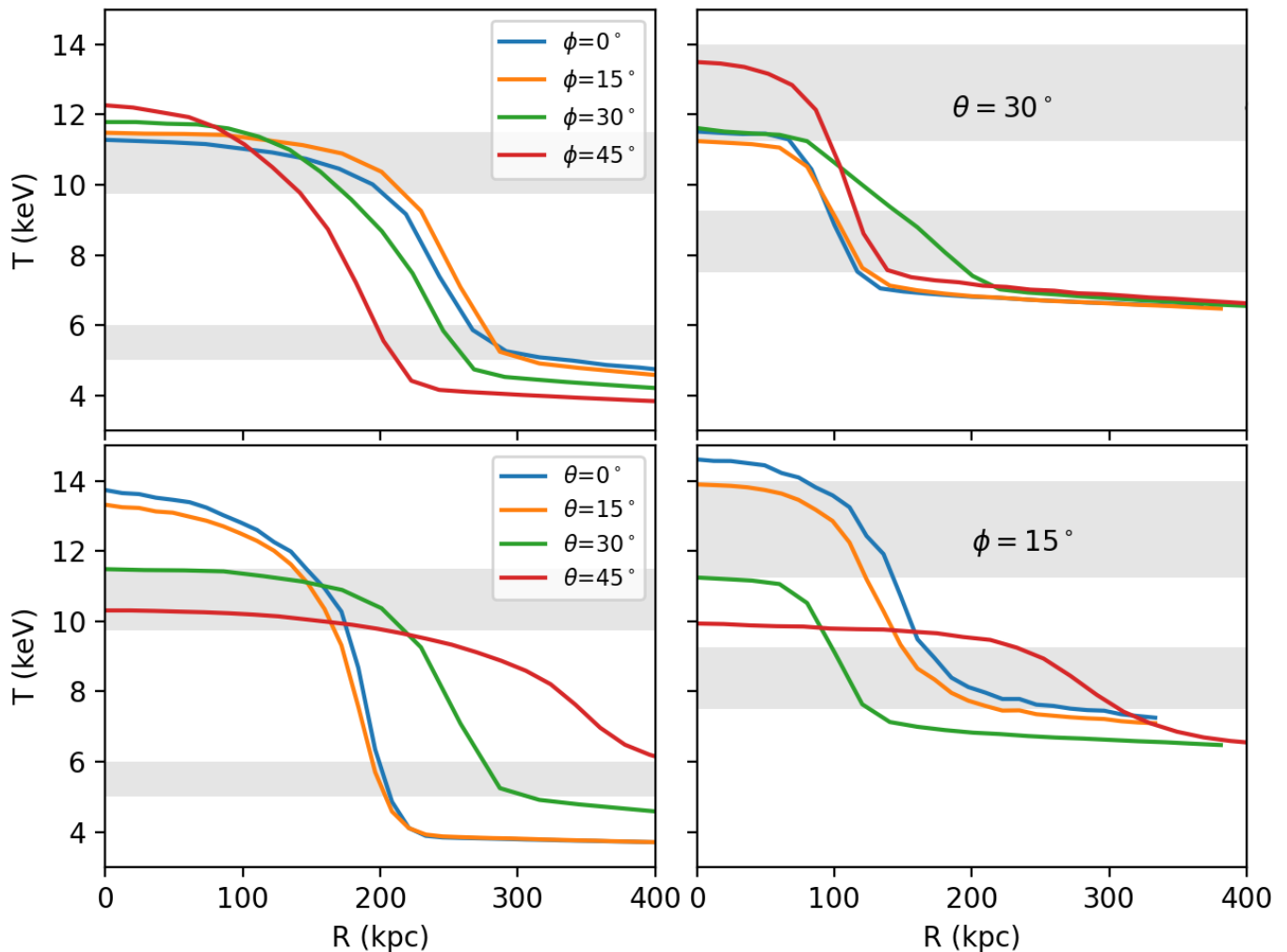


Figure 7. The temperature profiles of the bow (left) and upstream (right) shocks for different viewing directions. The top panels hold $\theta = 30^\circ$ and vary ϕ , while the bottom panels hold $\phi = 15^\circ$ and vary θ . The shaded grey regions show the $1\text{-}\sigma$ error bars on the pre- and post-shock temperatures for the corresponding shocks from Russell et al. (2012).

eter tests, we chose to zoom in on the region around a primary cluster mass $M_1 = 6 \times 10^{14} M_\odot$, a mass ratio $R = 1 : 3$, an impact parameter $b = 100$ kpc, and initial relative velocity $v_{rel} = 1500$ km/s. The following sections describe the zoomed in region of parameter space, so as to focus on systems like Abell 2146.

4.2 Viewing direction

As shown in Fig. 1, the merger in our simulations occurs in the x-y plane of the simulation domain, with the initial relative velocities along the x-axis and initial impact parameter along the y-axis; this defines the so-called plane of the orbit. The default line-of-sight is in the z-direction, as is the angular momentum. Instead, if the observer views the system along some different direction, they would see a different projection of the 3D system. Each viewing direction is defined by viewing angles (θ, ϕ) , where θ is the polar angle and ϕ the azimuthal angle (see Fig. 1).

Fig. 6 illustrates the effect on the appearance of a simulation of changing the two viewing angles for a given snapshot.

For small values of ϕ , increasing θ (a) increases the apparent pre-shock temperature, (b) increases the stand-off distance between the cold front and the bow shock and (c) decreases the apparent offset between shocks. The latter effect is the smallest, because the two shocks have large radii of curvature. Increasing ϕ has a barely discernible effect for low θ , but as seen in the panels for $\theta \gtrsim 30^\circ$, counters the effect of changing θ alone. Each of these effects can be explained by simple geometric arguments.

The shocks form along the axis of motion of the substructure through the ICM, in the x-y plane, so their separation is maximal along that axis. The velocities of the two subclusters are also entirely in the x-y plane, so that if viewed along the z-axis, the line-of-sight velocity difference between the subclusters is 0. The unperturbed cluster is spherical, and the radius of curvature R_s of the shock front is smaller than its cluster-centric radial position r . The unshocked gas can be assumed to move at approximately the same speed around the shock front, but the jump conditions only apply to the component of the gas velocity perpendicular to the shock front at any point. The speed of the shock at each point on the front

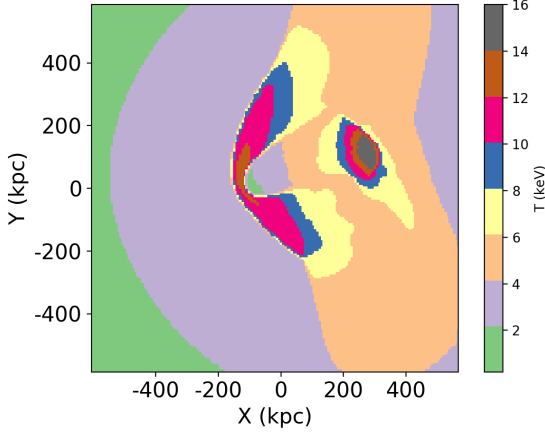


Figure 8. Temperature map for one of the snapshots similar to Abell 2146, using a discrete colormap to emphasise the gradient in pre-shock temperature. Changing the viewing angle would lead us to see the shock at a smaller distance from the primary cluster core, where the background temperature is higher. As a result, the shock will appear weaker.

is therefore $v \cos \eta$, where η is the angle between the normal to the front and the velocity of the front with respect to the gas; thus $\eta = 0^\circ$ at the leading edge of the shock. Changing the viewing direction generally moves the point where our line of sight is tangent to the shock front away from the leading edge of the shock, so that the observed shock strength is weaker. This additionally moves the tangent point to smaller r , increasing the preshock temperature at the tangent point. Finally, the radius of curvature R_c of the cold front is smaller than R_s . This means that the minimum separation between the two features, i.e., the standoff distance, is minimised in the plane of the merger, and increases for other viewing directions. Each of these phenomena can be understood intuitively as illustrated in Fig. 8, which shows a simulated temperature map with a discrete colormap to accentuate the difference in temperature depending on the position r .

Older simulation studies, tailored to the observing capabilities of telescopes like ROSAT, stated that the merger needs to be close to the plane of the sky for the shock features to be visible (e.g., Ensslin et al. 1998; Ricker 1998), although how close is not clearly defined. Fig. 6 shows, however, that both shock fronts are distinctly visible even for inclinations as high as ($\theta = 30^\circ, \phi = 15^\circ$). Therefore, the visibility of shocks does not constrain the merger axis to be very close to the plane of sky.

Instead, we need a more quantitative comparison, as shown in Fig. 7. Note that this is for $M_1 = 5 \times 10^{14} M_\odot$, $M_2 = 1.6 \times 10^{14} M_\odot$. Higher masses would increase the normalisation of the temperature profiles. The horizontal shaded areas show the $1-\sigma$ error bars on the pre- and post-shock temperatures for Abell 2146 (Russell et al, in prep.). From Fig. 6, we find that $\theta = 30^\circ$ produces the correct standoff distance at $\phi = 0$. The top panel of Fig. 7 shows the temperature profiles across the bow (left) and upstream (right) shocks for various values of ϕ at $\theta = 30^\circ$, with good matches to the observations for $\phi < 15^\circ$. The bottom panel then holds $\phi = 15^\circ$ and varies θ . In this way, we find that $\theta = 30^\circ$ matches observations. Lower values result in a post-shock temperature that is too high,

while higher values cause the shock to be much shallower than observed.

The standoff distance between the bow shock and the cold front also depends on the relative velocity, or, equivalently, the angular momentum of the merger. To break this degeneracy, we aim to additionally reproduce the observed line-of-sight velocity offset between the BCGs (White et al. 2015). Our simulations do not explicitly include cluster galaxies; however, BCGs are known to trace the potential minima of galaxy clusters (e.g., Zitrin et al. 2012, and references therein). The potential minima of the halos were identified using the `peak-local-max` function in the Scikit-Image Python package on the slice of the gravitational potential in the x - y plane. The velocity v of a BCG is estimated as the average velocity of all the dark matter particles within 50 kpc of its potential minimum; this radius is characteristic for BCGs of clusters of the masses considered (e.g., Lin & Mohr 2004, and references therein). The line-of-sight velocity difference between the BCGs depends on the viewing angle, as detailed in §2.2.

4.3 Total mass and mass ratio

Increasing the total mass, first of all, increases the overall projected temperature, since the thermal pressure now has to balance a greater weight of overlying gas. The Mazzotta-weighted average temperature of A2146 within a radius of 2 arcmin ($\simeq 440$ kpc), covering both the shocks, is 7.5 ± 0.3 keV if the cool core (of radius $10''$ or 37 kpc) is excised and 6.7 ± 0.3 keV if it is included (Russell et al. 2012). Simply by matching the limits of the colorbars in the observed and simulated maps of projected temperature, we can visually rule out systems whose average temperature is too small or too large. The core-excised (included) average temperatures for the 1:3 mass ratio mergers presented in Fig. 10 are 5.62 (5.15) for $M_{\text{tot}} = 6.6 \times 10^{14} M_\odot$, 7.33 (6.23) for $M_{\text{tot}} = 8.1 \times 10^{14} M_\odot$ and 8.10 (6.30) for $M_{\text{tot}} = 9.4 \times 10^{14} M_\odot$, where $M_{\text{tot}} = M_1 + M_2$ is the sum of the two total masses in the super-NFW formulation. The corresponding total virial masses are $(4.5, 5.4, 6.3) \times 10^{14} M_\odot$, with the middle value consistent with observed temperatures assuming that the merger occurs in the plane of the sky. Fig. 10 further reminds us that if the merger does not occur in the plane of the sky, the observed temperature is an underestimate. Therefore, a greater mass is possible if the viewing angles are larger.

Secondly, increasing the total mass increases the scale radii of the two halos. This means that for the same absolute magnitude of the impact parameter, greater fractions of the two cluster cores interact with each other during pericentre passage. In other words, increasing halo mass while holding impact parameter constant is equivalent to holding mass constant and reducing impact parameter, so that the cores are more disrupted. In the second row of Fig. 10, this is seen as a "fatter" bullet and a less prominent plume, either due to higher total mass at fixed mass ratio (top row), or higher mass ratio at fixed primary halo mass (second row). The acceleration due to increased halo mass also means that for the same initial relative speed in the simulation, the shocks produced at the best-fit snapshot are stronger. Fig. 9 additionally quantifies the difference between using different mass ratios but same mass for the primary halo, by plotting the temperature profiles out from the peak of the bow shock.

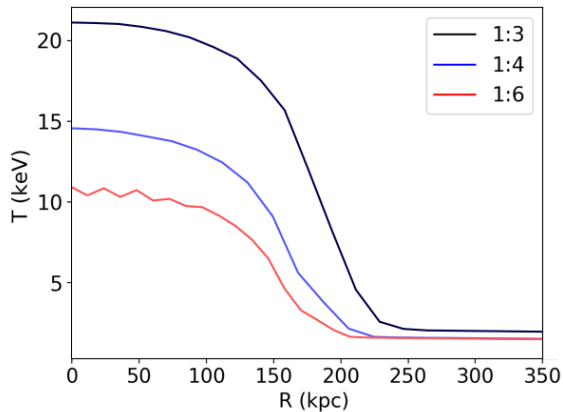


Figure 9. Projected temperature profiles of the bow shock for same primary halo mass but different mass ratios. Not only is the peak temperature significantly higher for a more massive secondary halo, but the shocked region is wider.

Increasing the mass of the secondary also increases ram pressure stripping of the secondary core. This can be seen in narrowing of the leading edge of the core, the formation of a stronger upstream shock, and a larger standoff distance. Based on the second row of Fig. 10, then, we favour a mass ratio of 1:3. The standoff distance is still lower than in observations, but, as discussed above, this can be fixed with a larger θ .

4.4 Impact parameter and initial relative speed

The X-ray observations rule out a perfectly head-on merger because the disrupted subcluster core is asymmetric. The head of the bullet is curved, and its tail fans out more towards the South than to the North. The greater the impact parameter, the greater this asymmetry. The appearance of this bullet is thus affected by the orientation of our line of sight with respect to the plane of the orbit. Fig. 6 showed this for the case $b = 100$ kpc. If viewed from sufficiently close to the plane of the orbit, the curvature of the bullet becomes very hard to perceive, and it becomes difficult to distinguish from a merger with a zero impact parameter. For larger b , however, the curvature of the bullet is too large to be erased by modest inclination of the merger plane with the plane of the sky. Furthermore, the core of the subcluster experiences very little ram pressure, and the cold front is much wider than observed. Similarly, the core of the primary cluster is less perturbed for larger b , leaving an intact core rather than a "plume". Given these effects, we can constrain $b \sim 100$ kpc.

As seen in the last panel of Fig. 10, increasing the relative velocity of the perturber increases the strength of the shock. The effect on the standoff distance is less linear. On the one hand, if the subcluster moves faster through the ICM, it stays closer to the bow shock, and this decreases the standoff distance. We see this effect as we increase v_{rel} from 720 to 1252 km/s. But increasing the velocity also increases the ram pressure, pushing gas from the subcluster core away from its direction of motion and increasing the standoff distance. This is what we see in further increasing v_{rel} to 2200 km/s. Given the observed strength and width of the upstream

shock, the intermediate speed of 1252 km/s is most likely; the observed standoff distance can then be increased by increasing θ , as is already encouraged by the analyses of total mass and mass ratio.

4.5 Dark matter concentration

A higher concentration for either cluster makes its core more compact and resistant to disruption. If the primary cluster is more concentrated, there is more gravitating mass enclosed within the core, and the subcluster bullet is accelerated more during infall. As a result, the gas in the subcluster experiences higher ram pressure $p_{ram} = \rho v^2$. This causes more gas to be swept away from the leading edge of the subcluster core, into a wake, which is undergoing a reverse shock. This has two observable consequences. Slowing the gas "bullet" increases the standoff distance between the bow shock and the cold front. At the same time, the gas displaced from the core of the infalling cluster impedes the gas infalling from further in its wake, boosting the strength and extent of the upstream shock. Both of these effects are shown in the top panel of Fig. 11. The bottom panel shows that the plume feature associated with the core of the primary halo is brighter and less disturbed if its concentration is higher. We find that the concentration of the subcluster, on the other hand, has no appreciable effect on the gas observables. Since other parameters affect the same observables much more dramatically, we find that c_2 is not well-constrained by X-ray imaging.

We note that this result is for mergers of the explored mass ratios, 1:3-1:6. If a merger is closer to equal mass, c_2 would have much the same effect as c_1 on the gas in the other merging component.

The standoff distance was smaller than observed for the parameters tested in Fig. 10, which all used $c_1 = 4.1$. A denser dark matter halo, like $c_1 = 5$, would solve this issue and remove the need for larger θ .

4.6 Gas profiles

The model in Eq. 3 contains two parameters that affect the compactness and cuspleness of the core - the core radius r_c and the central density slope α . The scale radius r_s and the outer slope parameters β and ϵ affect the outskirts, so we do not vary them in our study and just use the best-fit values from Vikhlinin et al. (2006).

It is important to note that r_c is a purely empirical parameter, which can be arbitrarily tuned in the Vikhlinin et al. (2006) formulation to match the data. We would like to choose core radii that produce profiles analogous to observed relaxed clusters (De Grandi & Molendi 2002; Vikhlinin et al. 2005; Hogan et al. 2017). As shown in Fig. 12, our profiles look like cool-cores, with high central densities and temperatures decreasing in the centre, for $\alpha = 0$, $r_c/a = 0.02$; for $\alpha = 0$, $r_c/a = 0.5$, they have lower, flat central densities and high central temperatures, like observed non-cool cores. While we acknowledge that the cores of clusters do not follow a strict dichotomy, we use these pairs of parameters when modelling each halo as a cool or non-cool core.

Fig. 13 shows that the X-ray images of the merger depend strongly on whether, per our modeling above, each cluster has a cool- or non-cool core. In the top panels, the primary

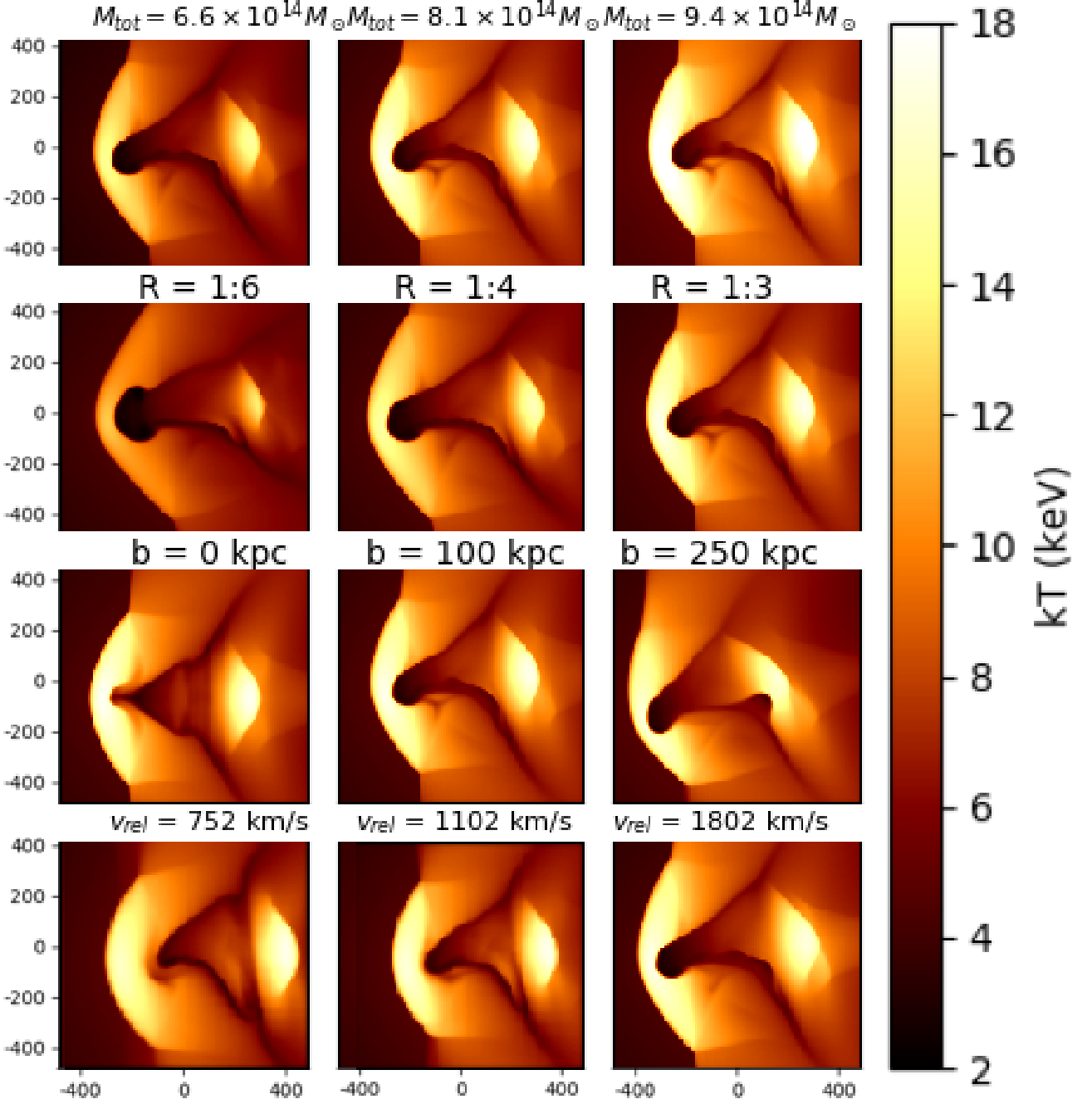


Figure 10. The effect of changing key dynamical parameters one at a time, holding all the others constant. *Top row:* Increasing the total mass of the system increases the temperature of the ICM as well as the shocks. *Second:* Increasing the mass of the secondary cluster, and therefore the mass ratio $R = M_1 : M_2$, increases the strength of the shocks as well as increasing the standoff distance. *Third:* Increasing the impact parameter b (in kpc), while holding all other parameters constant, curves the path of the secondary cluster core towards the primary core, creating a more arced cold front. The relative sizes and orientations of the different X-ray features are most significantly affected by b . *Bottom row:* Increasing the initial relative speed of the cluster centres increases the strengths of the shocks, but reduces the standoff distance and changes the radii of curvature of the shock fronts.

halo has a cool core, whereas in the bottom panels it has a non-cool core. Similarly, in the left panels the subcluster has a cool core, while on the right it has a non-cool core. The four scenarios are strikingly different. When either core is non-cool, it is more extended and more susceptible to stripping.

A cool-core secondary cluster will produce a bullet-like cold front; there is no low-entropy gas to form such a feature if it were a non-cool core. The remnant of the primary cluster core remains partially intact if it starts out as a cool-core, with the remainder drawn out into a plume-like shape if the

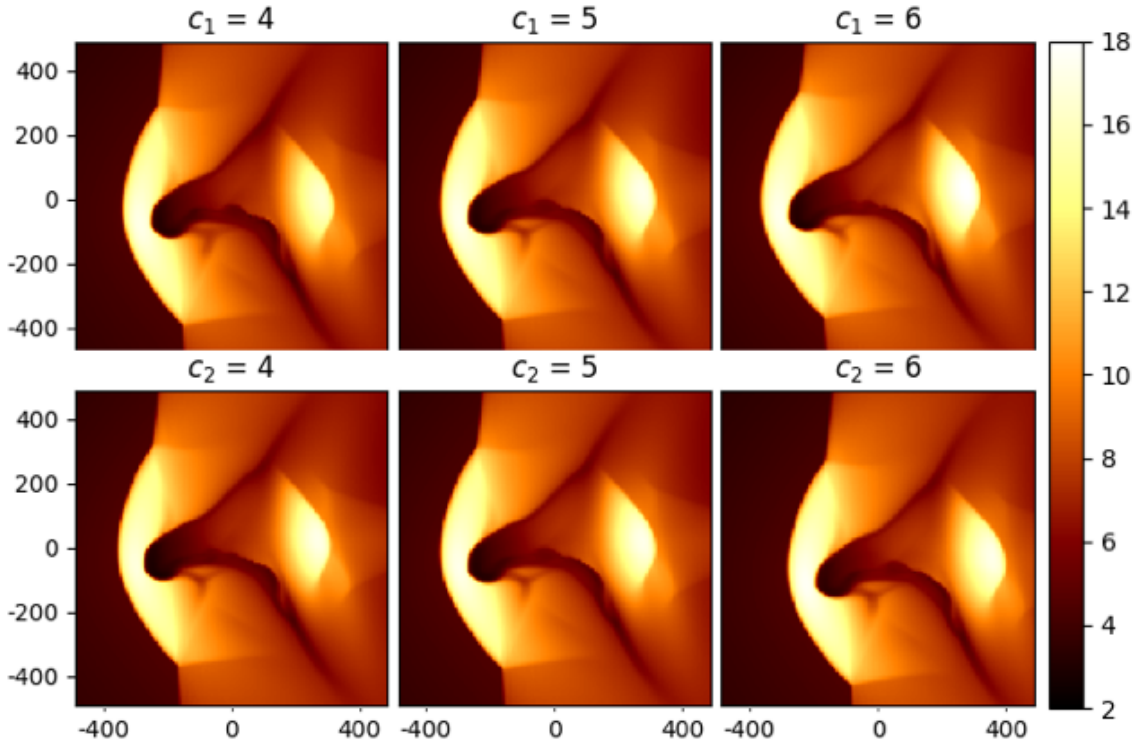


Figure 11. The effect of changing the dark matter concentration of the primary (top) and secondary (bottom) halo while holding all other parameters constant. A lower concentration for the primary, or a higher one for the secondary, results in more instabilities along the cold strip of gas connecting the two disrupted cores. We note that the details of KHI are sensitive to the presence of turbulence in the ICM, which we have not included. All other features remain unaffected.

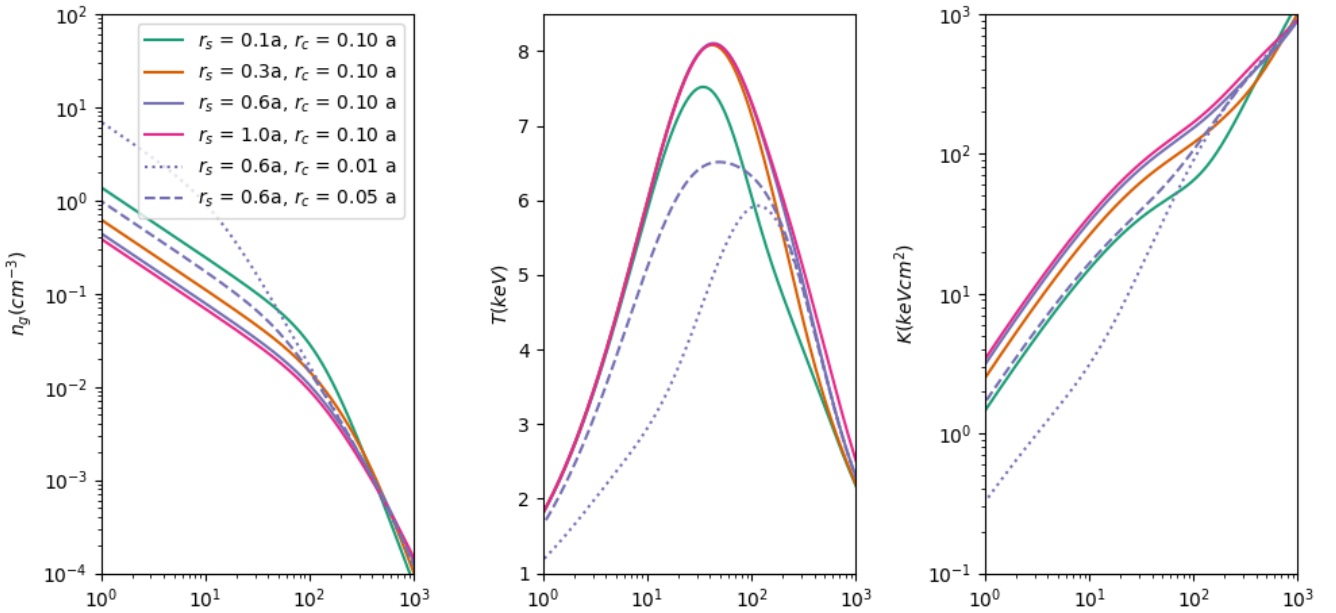


Figure 12. The effect of varying the gas scale radius r_s in Eq. 3 and core radius r_c for $\alpha = 2$. Here, $M_{sNFW} = 1.6 \times 10^{14} M_{\odot}$, $c_{NFW} = 5.2$, and $r_c = 0.1a$. Decreasing either the scale or core radius produces a denser, lower-entropy core. While there is a spread in observed cluster cores, we find that the cool core population is generally well fit with $\alpha = 2$, $r_c \sim 0.05a$ and $r_s = 0.6a$, so that the entropy decreases monotonically towards the centre. Through a similar comparison, we describe non-cool cores with $\alpha = 0$, $r_c \sim 0.3a$ and $r_s = 0.6a$.

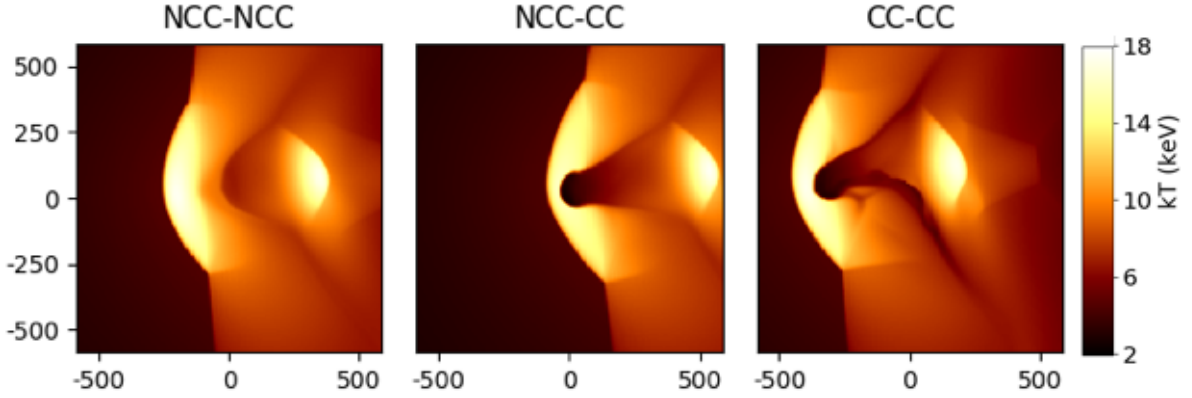


Figure 13. The morphology of the merger looks extremely different depending on whether each of the components has a cool or non-cool core. Here, both clusters are modeled with $\alpha = 0$; the cool cores have core radii $r_c = 0.02a$, and the non-cool cores have $r_c = 0.5a$, where a is the NFW scale radius. Abell 2146 clearly resembles a system where both components were initially cool-core clusters.

secondary also has a cool core, as seen in Abell 2146. If it is a non-cool core, there is no low-entropy material to start with and form the plume. We therefore conclude that both the primary and secondary clusters in Abell 2146 must have had cool cores before the merger. Small adjustments of r_c around the best-fit value of $0.02a$ then have very small effects on the width of the bullet (subcluster core remnant) and brightness and extent of the plume (primary cool remnant).

4.7 Best fit simulations for Abell 2146

Our simulations are consistent with the X-ray observations for a primary halo of virial mass $M_1 = 5.0 \times 10^{14} M_\odot$ and an infalling halo mass $M_2 = 1.6 \times 10^{14} M_\odot$, so that the mass ratio $R = 1:3$, observed 0.1 Gyr after pericenter passage. Both clusters initially have cool cores. The larger mass in each case would require the merger to be inclined with respect to the plane of the sky. The concentration of the more massive halo is ~ 5 , on the higher end of the scatter in the concentration-mass relation; the concentration of the subhalo does not visibly affect either the X-ray or lensing maps. The initial relative speed of the cluster centres was likely $v_{\text{rel}} \simeq 1200$ km/s, and impact parameter $b = 100$ kpc. The system is likely viewed from a direction of $\theta = 30^\circ$; $\phi = 15^\circ$ then reproduces the observed temperature profiles at the shock as well as the line-of-sight velocity offset between the BCGs.

5 DISCUSSION

5.1 Error bars including covariance

Although, in principle, an error region could be constructed for the model of A2146, this is not feasible with current computing resources. Since the parameters affect the same features in different ways, mapping out the interdependence of observed features on the parameters would require a large suite of simulations sampling many combinations of all the significant parameters, including M_1 , R , b , v , θ , ϕ , c_1 . This leaves us with a 7-dimensional space even after fixing the parameters c_2 , α_1 , and α_2 , which have less visible impact on the X-ray images. For each simulation in such a study, it will be important to quantify the similarity of each snapshot

to the observation. This would have to involve some combination of at least the shock separation, the standoff distance, the shock strengths, and the average temperature with and without the cool core. Even exploring just three values for each simulation yields over 2000 simulations, which cannot be inspected manually in the same way as in this pilot study. Instead, it would require a pipeline to compare simulations to observations and move in the parameter space. Nevertheless, here we have explored the physical impact of each of these parameters on a binary merger like A2146, demonstrating the observable impacts of each parameter on the system and providing a basis for the interpretation of similar systems in the future.

5.2 Resolution tests

We tested the effect of adding an additional refinement level, i.e., doubling the spatial resolution and octupling the mass resolution. Increasing the resolution primarily reduces numerical viscosity, permitting faster growth of fluid instabilities, notably the Kelvin-Helmholtz Instability (KHI). Indeed, Fig. 14 shows that the boundaries of the bullet-like cold front are more disrupted, and clear wave-like structures appear in the bridge connecting the two cool-core remnants. This will be significant in future studies that measure the plasma viscosity based on the development of KHI. It will also affect measurements of thermal conduction, which rely on the width of the contact discontinuities; this width cannot, of course, be lower than the simulation resolution. The distances between the features, however, remain unchanged, as do the temperature and velocity structures. Since these are the properties we use to constrain parameters in this study, we conclude that the hydrodynamic resolution of 6.8 kpc is sufficient. Reducing the number of dark matter particles by half also did not change the results; for similar studies in the future, we would recommend using this lower number of dark matter particles to reduce the simulation time by $\sim 40\%$.

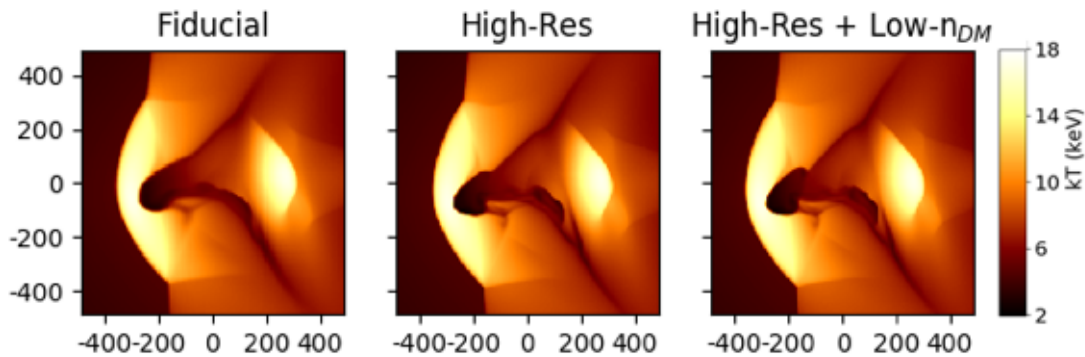


Figure 14. The effect of increasing the maximum refinement level (middle panel) and then halving the number of dark matter particles (right panel), in comparison with the resolution of this study (left panel). Doubling the hydrodynamic resolution increases the growth of fluid instabilities all along the cold discontinuities. However, the shock separation, standoff distance, average temperature, shock Mach numbers and the velocity offset between the BCGs remain unchanged. Reducing the force resolution by halving the number of dark matter particles has a negligible effect on the KHI.

6 CONCLUSIONS

We have performed a large suite of idealised simulations of binary mergers between galaxy clusters using the GPU-accelerated adaptive mesh refinement code GAMER-2, with the goal of constraining merger parameters using deep Chandra X-ray and lensing observations of Abell 2146. We assess the roles of halo masses, NFW concentrations, gas profiles, impact parameter, initial relative velocity, and viewing direction on observable quantities on X-ray properties and gravitational lensing observations. In searching for a simulated analog of the observed cluster merger Abell 2146, we find various results that will be helpful for any future interpretations of merging galaxy clusters. These will allow us to understand the laboratory, before using it as a test site for constraining cosmology and ICM microphysics. Our main findings are summarized as follows:

- The average temperature including and excluding the cool core pointed to a virial mass of $M_1 = 5.0 \times 10^{14} M_\odot$ for the primary halo and $1.6 \times 10^{14} M_\odot$ for the secondary halo.
- The large standoff distance favours an initial infall speed of $v_{\text{rel}} = 1150 \text{ km s}^{-1}$ and a viewing direction offset from the perpendicular to the plane of the merger (the z -axis) by about 30° in the initial direction of motion of the infalling subcluster [$\theta = 30^\circ$]. The observed strengths of the bow and upstream shocks are then reproduced for $15^\circ < \phi < 30^\circ$. This viewing direction also brings the simulated velocity offset between the cluster potential minima in agreement with the observed line-of-sight velocity difference of the BCGs.
- If the primary cluster has a cool core, it is more efficient at stripping the secondary core, resulting in a stronger and brighter upstream shock than if it had a non-cool core. If the secondary cluster has a cool core, it is more resilient to stripping, and disrupts the core of the primary cluster to form a plume-like feature. If instead it is a non-cool core, almost all the gas is stripped into an upstream shock behind the primary core, which in turn remains almost intact. We conclude that the cold "bullet" and "plume" features are the remnant cores of the secondary and primary clusters, respectively, if both clusters initially had cool cores and fell in with an impact parameter of $b = 100 \text{ kpc}$.
- Smaller subcluster masses, smaller initial relative veloc-

ities, and larger impact parameters all result in lower Mach numbers for the shocks.

- In principle, increasing the dark matter concentration of the primary halo slightly strengthens the upstream shock and increases the standoff distance of the bow shock, i.e., its separation from the cold front. This is because the bullet is slowed by the greater ram pressure. However, using $3 < c_{\text{NFW}} < 6$ for both clusters did not produce significant enough differences in the simulated X-ray images. Therefore, X-ray images alone are unable to constrain the dark matter concentrations of the halos.

- We find that the total mass of A2146 is significantly lower than previous determinations based on weak lensing data, and that (driven by the X-ray measurements) the more massive cluster is Abell 2146-B. The former factor can be explained since the parameterised models assumed NFW profiles with concentrations expected for relaxed cluster halos, whereas the core of the merging system is gravitationally compressed around pericentre passage, effectively increasing the concentration of the NFW model for each halo. Instead, it is important to consider lower halo masses than suggested from the earlier lensing analysis, and forward model using the simulations to obtain the synthetic lensing signal. That Abell 2146-A is the more massive cluster in the lensing analysis is still unexplained and is beyond the scope of this work.

This study paves the way for extracting more information from X-ray and optical observations for merging galaxy clusters. We have demonstrated how X-ray measurements alone can tightly constrain the halo masses even in a non-equilibrium system. The time since pericentre passage, impact parameter, dark matter concentration of the primary halo, and viewing direction can all be constrained using X-ray maps alone, and can be corroborated with optical measurements of BCG positions and velocities. The masses and velocities of merging clusters provide tests of cosmological models, which will be crucial in ongoing and upcoming surveys like eROSITA, DES, HSC, and Rubin. Once these hydrodynamic parameters have been constrained, a given merging cluster can then be used to study the nature of dark matter and ICM microphysics, such as viscosity, thermal conductivity, and magnetic field strength.

ACKNOWLEDGEMENTS

We thank the anonymous referee for their very helpful comments. We thank Rebecca Canning for her pointers on the dynamical and lensing observations of the system, and Miyoung Choi for guiding us through the lensing analysis pipelines. UC was supported as a Chandra Pre-Doctoral Fellow by NASA Grants G08-19110B and G08-19108X. JAZ and PEJN acknowledge support through Chandra Award Number G04-15088X issued by the Chandra X-ray centre, which is operated by the Smithsonian Astrophysical Observatory for and on behalf of NASA under contract NAS8-03060. SF and LJK acknowledge support for this work provided by the National Aeronautics and Space Administration through Chandra Award Number G08-19110D issued by the Chandra X-ray Center, which is operated by the Smithsonian Astrophysical Observatory for and on behalf of the National Aeronautics Space Administration under contract NAS8-03060. The simulations were run on the Grace HPC cluster at the Yale Centre for Research Computing.

DATA AVAILABILITY

Snapshots of the simulations used for this project will sequentially be added to the Cluster Merger catalog (ZuHone et al. 2018), accessible at <http://gcmc.hub.yt/>. The full simulation files are too large to host permanently on a server, and will be shared on reasonable request to the corresponding author.

REFERENCES

- Avestruz C., Nagai D., Lau E. T., Nelson K., 2015, *ApJ*, **808**, 176
 Brunetti G., Jones T. W., 2014, *International Journal of Modern Physics D*, **23**, 1430007
 Canning R. E. A., et al., 2012, *MNRAS*, **420**, 2956
 Clowe D., Bradač M., Gonzalez A. H., Markevitch M., Randall S. W., Jones C., Zaritsky D., 2006, *ApJ*, **648**, L109
 Coleman J. E., et al., 2017, *MNRAS*, **464**, 2469
 De Grandi S., Molendi S., 2002, *ApJ*, **567**, 163
 Duffy A. R., Schaye J., Kay S. T., Dalla Vecchia C., 2008, *MNRAS*, **390**, L64
 Eddington A. S., 1916, *MNRAS*, **76**, 572
 Ensslin T. A., Biermann P. L., Klein U., Kohle S., 1998, *A&A*, **332**, 395
 Fakhouri O., Ma C.-P., Boylan-Kolchin M., 2010, *MNRAS*, **406**, 2267
 Fruscione A., et al., 2006, CIAO: Chandra’s data analysis system. p. 62701V, [doi:10.1117/12.671760](https://doi.org/10.1117/12.671760)
 Golovich N., Dawson W. A., Wittman D., Ogreaan G., van Weeren R., Bonafede A., 2016, *ApJ*, **831**, 110
 Golovich N., van Weeren R. J., Dawson W. A., Jee M. J., Wittman D., 2017, *ApJ*, **838**, 110
 Harvey D., Massey R., Kitching T., Taylor A., Tittley E., 2015, *Science*, **347**, 1462
 Hogan M. T., et al., 2017, *ApJ*, **851**, 66
 Kahlhoefer F., Schmidt-Hoberg K., Frandsen M. T., Sarkar S., 2014, *MNRAS*, **437**, 2865
 Kazantzidis S., Magorrian J., Moore B., 2004, *ApJ*, **601**, 37
 Kim S. Y., Peter A. H. G., Wittman D., 2017, *MNRAS*, **469**, 1414
 King L. J., et al., 2016, *MNRAS*, **459**, 517
 Lacey C., Cole S., 1993, *MNRAS*, **262**, 627
 Lage C., Farrar G. R., 2015, *J. Cosmology Astropart. Phys.*, **2015**, 038
 Lilley E. J., Evans N. W., Sanders J. L., 2018, *MNRAS*, **476**, 2086
 Lin Y.-T., Mohr J. J., 2004, *ApJ*, **617**, 879
 Lokas E. L., Mamon G. A., 2001, *MNRAS*, **321**, 155
 Markevitch M., Vikhlinin A., 2007, *Phys. Rep.*, **443**, 1
 Markevitch M., Gonzalez A. H., David L., Vikhlinin A., Murray S., Forman W., Jones C., Tucker W., 2002, *ApJ*, **567**, L27
 Markevitch M., et al., 2003, *ApJ*, **586**, L19
 Markevitch M., Gonzalez A. H., Clowe D., Vikhlinin A., Forman W., Jones C., Murray S., Tucker W., 2004, *ApJ*, **606**, 819
 Massey R., et al., 2015, *MNRAS*, **449**, 3393
 Massey R., et al., 2018, *MNRAS*, **477**, 669
 Mazzotta P., Rasia E., Moscardini L., Tormen G., 2004, *MNRAS*, **354**, 10
 Navarro J. F., Frenk C. S., White S. D. M., 1996, *ApJ*, **462**, 563
 Neto A. F., et al., 2007, *MNRAS*, **381**, 1450
 Planck Collaboration et al., 2016, *A&A*, **594**, A13
 Poole G. B., Fardal M. A., Babul A., McCarthy I. G., Quinn T., Wadsley J., 2006, *MNRAS*, **373**, 881
 Randall S. W., Markevitch M., Clowe D., Gonzalez A. H., Bradač M., 2008, *ApJ*, **679**, 1173
 Ricker P. M., 1998, *ApJ*, **496**, 670
 Ricker P. M., Sarazin C. L., 2001, *ApJ*, **561**, 621
 Ritchie B. W., Thomas P. A., 2002, *MNRAS*, **329**, 675
 Robertson A., Massey R., Eke V., 2017, *MNRAS*, **465**, 569
 Roediger E., Zuhone J. A., 2012, *MNRAS*, **419**, 1338
 Roediger E., Kraft R. P., Forman W. R., Nulsen P. E. J., Churazov E., 2013, *ApJ*, **764**, 60
 Roettiger K., Burns J. O., Loken C., 1996, *ApJ*, **473**, 651
 Roettiger K., Loken C., Burns J. O., 1997, *ApJS*, **109**, 307
 Rudd D. H., Nagai D., 2009, *The Astrophysical Journal*, 701
 Russell H. R., Sanders J. S., Fabian A. C., Baum S. A., Donahue M., Edge A. C., Mcnamara B. R., Odea C. P., 2010, *Monthly Notices of the Royal Astronomical Society*
 Russell H. R., et al., 2012, *MNRAS*, **423**, 236
 Sarazin C. L., 2002, in Feretti L., Gioia I. M., Giovannini G., eds, *Astrophysics and Space Science Library Vol. 272, Merging Processes in Galaxy Clusters*. pp 1–38 ([arXiv:astro-ph/0105418](https://arxiv.org/abs/astro-ph/0105418)), [doi:10.1007/0-306-48096-4_1](https://doi.org/10.1007/0-306-48096-4_1)
 Schive H.-Y., ZuHone J. A., Goldbaum N. J., Turk M. J., Gaspari M., Cheng C.-Y., 2018, *MNRAS*, **481**, 4815
 Schmidt W., Byrohl C., Engels J. F., Behrens C., Niemeyer J. C., 2017, *MNRAS*, **470**, 142
 Springel V., Farrar G. R., 2007, *MNRAS*, **380**, 911
 Takizawa M., 2005, *ApJ*, **629**, 791
 Tulin S., Yu H.-B., 2018, *Phys. Rep.*, **730**, 1
 Vikhlinin A., Markevitch M., Murray S. S., Jones C., Forman W., Van Speybroeck L., 2005, *ApJ*, **628**, 655
 Vikhlinin A., Kravtsov A., Forman W., Jones C., Markevitch M., Murray S. S., Van Speybroeck L., 2006, *ApJ*, **640**, 691
 Wang Q. H. S., Giacintucci S., Markevitch M., 2018, *ApJ*, **856**, 162
 White J. A., et al., 2015, *MNRAS*, **453**, 2718
 Wittman D., Cornell B. H., Nguyen J., 2018, *ApJ*, **862**, 160
 Zhang C., Churazov E., Forman W. R., Jones C., 2019, *MNRAS*, **482**, 20
 Zhang C., Churazov E., Dolag K., Forman W. R., Zhuravleva I., 2020, *MNRAS*, **494**, 4539
 Zitrin A., Bartelmann M., Umetsu K., Oguri M., Broadhurst T., 2012, *MNRAS*, **426**, 2944
 ZuHone J. A., 2011, *ApJ*, **728**, 54
 ZuHone J. A., Markevitch M., Ruzsowski M., Lee D., 2013, *ApJ*, **762**, 69
 ZuHone J. A., Kunz M. W., Markevitch M., Stone J. M., Biffi V., 2015, *ApJ*, **798**, 90
 ZuHone J. A., Kowalik K., Öhman E., Lau E., Nagai D., 2018, *ApJS*, **234**, 4
 Zuhone J. A., Roediger E., 2016, *Journal of Plasma Physics*, **82**, 535820301

Zuhone J. A., Markevitch M., Lee D., 2011, [The Astrophysical Journal](#), 743, 16